The fully non-linear post-Friedmann frame-dragging vector potential: magnitude and time evolution from *N*-body simulations

Daniel B. Thomas,[1,2]* Marco Bruni[1] and David Wands[1]

[1]*Institute of Cosmology and Gravitation, University of Portsmouth, Dennis Sciama Building, Burnaby Road, Portsmouth PO1 3FX, UK*
[2]*Department of Physics, University of Cyprus, Aglantzia, 2109 Nicosia, Cyprus*

ABSTRACT

Newtonian simulations are routinely used to examine the matter dynamics on non-linear scales. However, even on these scales, Newtonian gravity is not a complete description of gravitational effects. A post-Friedmann approach shows that the leading-order correction to Newtonian theory is a vector potential in the metric. This vector potential can be calculated from *N*-body simulations, requiring a method for extracting the velocity field. Here, we present the full details of our calculation of the post-Friedmann vector potential, using the Delaunay Tessellation Field Estimator code. We include a detailed examination of the robustness of our numerical result, including the effects of box size and mass resolution on the extracted fields. We present the power spectrum of the vector potential and find that the power spectrum of the vector potential is $\sim 10^5$ times smaller than the power spectrum of the fully non-linear scalar gravitational potential at redshift zero. Comparing our numerical results to perturbative estimates, we find that the fully non-linear result can be more than an order of magnitude larger than the perturbative estimate on small scales. We extend the analysis of the vector potential to multiple redshifts, showing that this ratio persists over a range of scales and redshifts. We also comment on the implications of our results for the validity and interpretation of Newtonian simulations.

Key words: gravitation – cosmology: theory – large-scale structure of Universe.

1 INTRODUCTION

On the largest scales in cosmology, theoretical calculations can be carried out using standard cosmological perturbation theory. These calculations fully encompass General Relativity (GR) but are limited to scales where the perturbations, in particular the density perturbation, are small. On smaller scales, where the focus is on non-linear structure formation, Newtonian *N*-body simulations are used. These simulations do not require that the density contrast be small, but they suffer from the limitations of being Newtonian rather than GR simulations. There is an entire field in cosmology dedicated to developing, running and analysing these Newtonian *N*-body simulations. There has been sporadic interest in understanding the use of Newtonian theory in cosmology (Tomita 1991; Shibata & Asada 1995; Matarrese & Terranova 1996; Takada & Futamase 1997; Carbone & Matarrese 2005; Hwang, Noh & Puetzfeld 2008; Flender & Schwarz 2012; Haugg, Hofmann & Kopp 2012; Hwang & Noh 2013; Kopp, Uhlemann & Haugg 2014; Milillo et al. 2015), as well as examining the relativistic interpretation of the simulations

(Chisari & Zaldarriaga 2011; Green & Wald 2012; Adamek et al. 2013; Bruni, Thomas & Wands 2014). These studies have predominantly focused on whether the dynamics of density contrast and scalar potential accurately match those of GR.

In this paper, we are mostly interested in another important limitation of Newtonian simulations. Even if the matter dynamics are being computed correctly, there are cosmological quantities of interest on non-linear scales that have no counterpart in Newtonian theory. Examples of these quantities include the difference between the two scalar potentials, gravitational waves and the vector potential in the metric, all of which must exist on non-linear scales in a GR universe.

These extra quantities would naively be expected to be small if the Newtonian simulations are a good approximation to a GR universe. However, explicitly calculating these quantities has several advantages. To start with, it would be good to have a quantitative check of whether these quantities are small, and indeed how small they are. In particular, as we enter the era of precision cosmology, we need to check that these quantities will not affect the observables at the per cent level. Furthermore, checking that these quantities are negligible provides a quantitative check on the Newtonian approximation in a Λ cold dark matter (ΛCDM) cosmology.

* E-mail: thomas.daniel@ucy.ac.cy

We will be working with the post-Friedmann formalism (Milillo 2010; Milillo et al. 2015). This generalizes to cosmology the weak-field (post-Minkowski) approximation, with a post-Newtonian style expansion (Chandrasekhar 1965; Weinberg 1972; Poisson & Will 2014) in inverse powers of the speed of light c of the perturbative quantities. These expansions need to be performed differently in cosmology compared to those in the Solar system due to the different situations and aims in the two cases. For example, the time–time and space–space components of the metric need to be treated at the same order in cosmology in order for the resulting equations to be a consistent solution of the Einstein equations.

The post-Friedmann formalism, when linearized, correctly reproduces conventional linear perturbation theory and can thus describe structure formation on the largest scales. More importantly, the leading-order equations in the $1/c$ expansion can be examined and are expected to yield the non-linear Newtonian equations. Note that in this 'Newtonian' regime, the density contrast has not been assumed to be small. The equations in this regime will be shown in Section 2, essentially comprising the Newtonian equations, as expected, plus an additional equation. This additional equation shows how the vector potential in the metric, the lowest order beyond-Newtonian quantity, is generated by the matter dynamics. This vector potential is the beyond-Newtonian quantity that we will examine in this paper; it is the cosmological manifestation of the ubiquitous relativistic effect of frame dragging. This effect has been measured in the Solar system by Gravity Probe B (Everitt et al. 2011).

In this paper, we present a calculation of this vector potential based on extracting the density and velocity fields from N-body simulations. We expand on the results of Bruni et al. (2014), which was the first calculation of an intrinsically relativistic quantity on fully non-linear scales from large-scale cosmological matter fields, rather than from individual astrophysical occurrences. The main focus in this paper is to present the method used to extract this vector potential from N-body simulations. In particular, we examine the robustness of the numerical extraction of the vector potential and present the tests we carried out to examine the numerical effects of simulation parameters on the extraction, which were not presented in Bruni et al. (2014).

The main physical results of this paper are Figs 3 and 8, showing the power spectrum of the vector potential at redshift zero and its evolution with time, respectively. Additionally, we have presented the ratio of the vector potential power spectrum to that of the scalar potential in Figs 5 and 9. The results on the magnitude and evolution of the power spectrum of the vector potential in this paper were used in Thomas, Bruni & Wands (2014) to examine the possible weak-lensing consequences of the vector potential.

This paper is laid out as follows. In Section 2, we present the pertinent details of the post-Friedmann formalism and show the equation governing the vector potential. We will also present our definitions and notation regarding vector power spectra. In Section 3, we explain how the relevant fields were extracted from N-body simulations and examine the robustness of this extraction. In Section 4, we show the power spectrum of the vector gravitational potential and its time evolution, as well as comparing it to the closest analytical results in the literature. We conclude in Section 5. Appendix A contains some details about vector power spectra and in Appendix B we show results from some of the numerical tests that were carried out. Additional plots are available as online supplementary material, divided amongst three files: Resolution_and_BoxSize_Dependence.pdf (hereafter RB), Grid-Size_and_Binning_Dependence.pdf (hereafter GB) and ConsistencyChecks.pdf (hereafter CC).

2 POST-FRIEDMANN FORMALISM

The post-Friedmann approach is developed in Milillo et al. (2015) and Milillo (2010); see there for the full details. This approach considers a dust (pressureless matter) cosmology with a cosmological constant. The perturbed Friedmann–Lemaître–Robertson–Walker metric, in Poisson gauge, is expanded up to order c^{-5}, keeping the g_{00} and g_{ij} scalar potentials at the same order:

$$g_{00} = -\left[1 - \frac{2U_\mathrm{N}}{c^2} + \frac{1}{c^4}\left(2U_\mathrm{N}^2 - 4U_\mathrm{P}\right)\right]$$

$$g_{0i} = -\frac{aB_i^\mathrm{N}}{c^3} - \frac{aB_i^\mathrm{P}}{c^5}$$

$$g_{ij} = a^2\left[\left(1 + \frac{2V_\mathrm{N}}{c^2} + \frac{1}{c^4}\left(2V_\mathrm{N}^2 + 4V_\mathrm{P}\right)\right)\delta_{ij} + \frac{h_{ij}}{c^4}\right]. \quad (1)$$

The g_{00} and g_{ij} scalar potentials have been split into the Newtonian (U_N, V_N) and post-Friedmann (U_P, V_P) components. Similarly, the vector potential has been split up into B_i^N and B_i^P. Since this metric is in the Poisson gauge, the three-vectors B_i^N and B_i^P are divergenceless, $B_{i,i}^\mathrm{N} = 0$ and $B_{i,i}^\mathrm{P} = 0$. In addition, h_{ij} is transverse and tracefree, $h_i^i = h_{ij}^i = 0$. Note that at this order, h_{ij} is not dynamical, so it does not represent gravitational waves. From a post-Friedmann viewpoint, there are two different levels of perturbations in the theory, corresponding to terms of orders c^{-2} and c^{-3}, or of orders c^{-4} and c^{-5}, respectively. Defining 'resummed' variables, such as $\Phi = 2U_\mathrm{N} + c^{-2}\left(2U_\mathrm{N}^2 - 4U_\mathrm{P}\right)$, then calculating the Einstein equations and linearizing them reproduces linear GR perturbation theory in Poisson gauge. Thus, this approach is capable of describing structure formation on the largest scales.

For smaller scales, in a dust cosmology, we are interested in the weak-field, slow motion, sub-horizon, quasi-static and negligible pressure regime. This is simply derived by retaining only the leading-order terms in the c^{-1} expansion and upon doing so we recover Newtonian cosmology, albeit with a couple of subtleties. The first is that the space–time metric is a well-defined approximate solution of the Einstein equations. The second is that we have an additional equation, which is a constraint equation for the vector gravitational potential B_i^N. The full system of equations obtained from the Einstein and hydrodynamic equations (Milillo et al. 2015), given the evolution of the background $a(t)$, is as follows:

$$\frac{\mathrm{d}\delta}{\mathrm{d}t} + \frac{v_{,i}^i}{a}\left(1 + \delta\right) = 0 \quad (2)$$

$$\frac{\mathrm{d}v_i}{\mathrm{d}t} + \frac{\dot{a}}{a}v_i = \frac{1}{a}U_{\mathrm{N},i} \quad (3)$$

$$\frac{1}{c^2 a^2}\nabla^2 V_\mathrm{N} = -\frac{4\pi G}{c^2}\rho_b\delta \quad (4)$$

$$\frac{2}{c^2 a^2}\nabla^2\left(V_\mathrm{N} - U_\mathrm{N}\right) = 0 \quad (5)$$

$$\frac{1}{c^3}\left[\frac{2\dot{a}}{a^2}U_{\mathrm{N},i} + \frac{2}{a}\dot{V}_{\mathrm{N},i} - \frac{1}{2a^2}\nabla^2 B_i^\mathrm{N}\right] = \frac{8\pi G\rho_b}{c^3}\left(1 + \delta\right)v_i. \quad (6)$$

As expected, we have the Newtonian continuity and Euler equations from the hydrodynamic equations as well as Poisson equation from the Einstein equations. Note that the time derivative here is the convective derivative, $\mathrm{d}A/\mathrm{d}t = \partial A/\partial t + v^i A_{,i}/a$, for any quantity A. The Einstein equations yield two additional equations. The first

is an equation forcing the scalar potentials V_N and U_N to be equal, consistent with there being only one scalar potential in Newtonian theory. Note that some approaches consider the potentials to be a priori equal at leading order whereas here we assumed that the full generality of GR and the equality of the potentials arose naturally on taking the Newtonian regime. The second additional equation relates the leading-order vector gravitational potential, B_i^N, to the momentum of the matter. Thus, even in the regime where the matter dynamics are correctly described by Newtonian theory, the frame-dragging potential B_i^N should not be set to zero; this would correspond to putting an extra constraint on the Newtonian dynamics. We note that there is a similar equation in several other formalisms in the literature (Takada & Futamase 1997; Green & Wald 2012; Hwang & Noh 2013). We can see from equation (6) that the potential B_i^N is sourced by the vector part of the energy current $\rho \boldsymbol{v}$. This is made apparent by taking the curl of this equation, which gives

$$\nabla \times \nabla^2 \boldsymbol{B}^N = -\left(16\pi G \rho_b a^2\right) \nabla \times \left[(1+\delta)\boldsymbol{v}\right], \qquad (7)$$

where the source term on the right-hand side splits up into three terms: the vorticity $\nabla \times \boldsymbol{v}$ and then two further terms,

$$\nabla \times \left[(1+\delta)\boldsymbol{v}\right] = \nabla \times \boldsymbol{v} + \delta \nabla \times \boldsymbol{v} + \nabla \delta \times \boldsymbol{v}. \qquad (8)$$

It is equation (7) that will be used for the rest of the paper. Since the matter dynamics are not affected at this order, i.e. they are described by the standard Newtonian equations (2)–(4), the density and velocity fields sourcing the vector potential are Newtonian and can be extracted from *N*-body simulations. Using the definitions of vector power spectra in Appendix A, the power spectrum of the vector potential is given by

$$P_{B^N}(k) = \left(\frac{16\pi G \rho_b a^2}{k^2}\right)^2 \frac{1}{k^2} P_{\delta v}(k), \qquad (9)$$

with

$$P_{\delta v} = P_{\nabla \times v}(k) + P_{\delta \nabla \times v}(k) + P_{(\nabla \delta) \times v}(k) + P_{(\nabla \times v)(\nabla \times v)}(k)$$
$$+ P_{(\nabla \delta \times v)(\delta \nabla \times v)}(k) + P_{(\delta \nabla \times v)(\nabla \times v)}(k). \qquad (10)$$

Unless stated otherwise, all plots of the gravitational potentials show the dimensionless power spectrum $\Delta(k)$; see Appendix A for conventions.

3 SIMULATIONS

Our simulations have all been run using the publicly available *N*-body code GADGET2 (Springel 2005). Many simulations have been run in order to quantify the effects of box size and mass resolution on the quantities that we are extracting; see Table 1 for a full list of the simulations. All of the simulations were run with dark matter particles only, as the equation for the vector potential is derived for a pressureless matter and cosmological constant cosmology. To allow comparison to previous studies of vorticity (Pueblas & Scoccimarro 2009), the simulations were run with the cosmological parameters $\Omega_m = 0.27$, $\Omega_\Lambda = 0.73$, $\Omega_b = 0.046$, $h = 0.72$, $\tau = 0.088$, $\sigma_8 = 0.9$ and $n_s = 1$. All of the simulations started at redshift 50 and had their initial conditions created using 2LPTIC (Crocce, Pueblas & Scoccimarro 2006). Our final result for the vector potential is taken from the three $160\,h^{-1}$ Mpc simulations with 1024^3 particles; these will be referred to as the high-resolution (HR) simulations.

Table 1. Parameters for the simulations.

Box size (h^{-1} Mpc)	Particle number	Mass resolution (10^8 M$_\odot$)	Number of realizations	Softening (h^{-1} kpc)
80	512^3	3.97	8	6.25
80	512^3	3.97	1	4.0
140	768^3	6.31	8	6.25
140	560^3	16.3	8	6.25
160	1024^3	3.97	3	6.25
160	880^3	6.26	3	6.25
160	640^3	16.3	8	6.25
160	640^3	16.3	1	5.0
160	320^3	130	8	15.0
200	1024^3	7.76	2	6.25
240	960^3	16.3	3	6.25
240	480^3	130	8	15.0
320	640^3	130	8	15.0

3.1 Tessellation

To extract the necessary fields from the simulations, the Delaunay Tessellation Field Estimator (DTFE) code was used (Cautun & van de Weygaert 2011). Standard methods of extracting fields from *N*-body simulations, such as cloud-in-cells (CiC; Hockney & Eastwood 1981), work well for the density field, as the particles, by definition, sample the density field well. However, these methods have several shortcomings when applied to the extraction of velocity fields. One is that the field is only sampled where there are particles, so in a low-density region the velocity field is artificially set to zero. In addition, the extracted field will be a mass-weighted, rather than volume-weighted field. A consequence of these shortcomings is that, as the grid size is increased, the velocity field will not converge. In fact, it will become zero in an increasing proportion of the grid cells as the grid size increases. Several authors have looked at using the Delaunay tessellation (Bernardeau & van de Weygaert 1996; Schaap & van de Weygaert 2000; van de Weygaert & Schaap 2009) for astrophysical applications including the examination of velocity fields. See also Pueblas & Scoccimarro (2009) for comparisons of extracting velocity fields with tessellations rather than more standard methods. The DTFE code constructs the Delaunay tessellation of the set of particles, consisting of tetrahedra whose nodes are located at the particles' positions. The tetrahedra are constructed such that the circumsphere of each tetrahedron does not contain any of the particles except for the particles located at the nodes of the tetrahedron in question. This makes the tessellation unique. The particles' velocities are then linearly interpolated across each tetrahedron, yielding a value for the smoothed velocity field and its gradients at every point in the simulation volume. A regular N_{grid}^3 grid is laid down and the code samples $N_{samples}$ points at random in each grid cell and averages the field over these points, giving a value for the smoothed field in each grid cell. Once the fields are obtained on the regular grid, the power spectra are calculated using the standard process of averaging the modulus-squared of the Fourier coefficients over a given range of k. For the analyses here, we used $N_{grid}/4$ bins, although varying this value does not affect the results (see Appendix B7).

3.2 Convergence and tests

It is important to ensure that our numerical result for the vector potential is robust and independent of the simulation parameters. In this subsection, we will present the results of our examination into the effects of different simulation parameters on the extracted
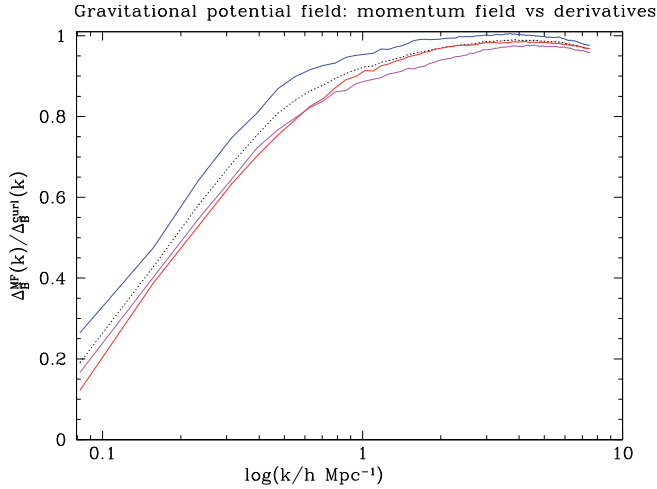
Figure 1. The ratio of the vector potential power spectra computed using the vector part of the momentum field and the curl of the momentum field. The blue, magenta and red curves show the ratio for the three realizations of the HR simulations, and the black (dashed) curve shows the average over these three. There is reasonable agreement between the two power spectra for the smaller scales; however, the two methods diverge for the largest scales and there is a difference of a factor of 5 at the largest scales. For most of the range of k under consideration ($k \geq 0.2\, h\ \mathrm{Mpc}^{-1}$), the two vector power spectra agree to within a factor of 2.

Figure 2. The ratio of the vector potential power spectra computed using the vector part of the momentum field calculated using the CiC method and the DTFE method. The blue, magenta and red curves show the ratio for the three realizations of the HR simulations, and the black curve shows the average over these three. The two methods agree very well on larger scales, but diverge for the smallest scales.

vector power spectrum. Since the velocity and density fields both contribute to the source for the vector potential, we will examine the density, vorticity and velocity divergence spectra too. We will examine their behaviour individually, compare them to other studies and methods of extraction and also consider the consistency of the extracted fields through the relations

$$k^2 P_\delta(k) = P_{\nabla \delta}(k)$$

$$k^2 P_v(k) = P_{\nabla \cdot v}(k) + P_{\nabla \times v}(k). \tag{11}$$

The box size and mass resolution of the simulation are the two main parameters whose effect on the extracted fields needs to be examined. In addition, we have examined the effect of varying the grid size and N_{samples}, which are both internal DTFE parameters. The parameters of the different simulations used are given in Table 1. We chose the softening lengths of the *N*-body simulations to be consistent with Pueblas & Scoccimarro (2009) in order to recreate their study of the velocity divergence and vorticity; however, varying the softening length did not influence the results, see Appendix B5.

Although we did run some simulations with a box size below 140 h^{-1} Mpc, we have not included these in the analysis here as smaller box sizes have systematically less power. See Appendix B6 for the results from these simulations and how they compare to the larger box sizes. For further results regarding the effects of a small simulation box on cosmological quantities, see Bagla & Prasad (2006), Bagla & Ray (2005) and Gelb & Bertschinger (1994).

3.2.1 A note on error bars

Since we have only three realizations of our HR simulations, we cannot compute meaningful error bars. Thus, we have not included any error bars in the majority of our plots. Instead, in Figs 1 , 2, 5 and 6, we have plotted the results from the three individual realizations, in order to illustrate by how much the results vary. Unless stated otherwise, the results shown in the other plots show the average over the
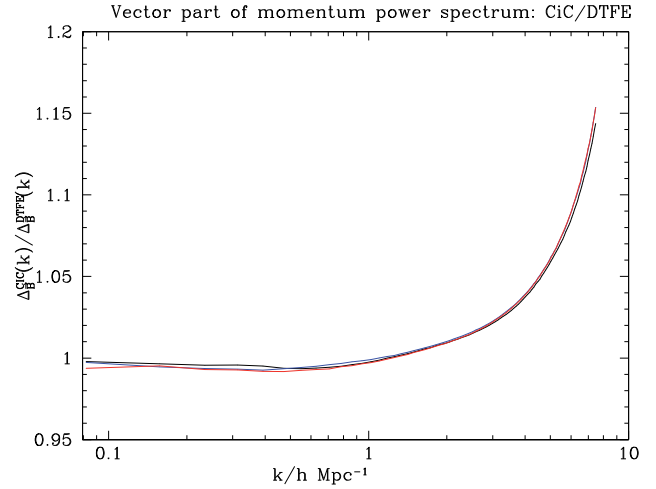
realizations. We explicitly examine the variation amongst realizations in Appendix B4 for several quantities, notably the vorticity and vector potential. In particular, we note there that when considering the vector potential, cosmic variance on the largest scales affects smaller scales, as explained by a perturbative analysis (Lu, Ananda & Clarkson 2008; Hui-Ching Lu et al. 2009). See Appendix B4 for more discussion of this. We also note there that the variation of the vorticity amongst realizations seems to be larger than the variation of the density, although there seems to be no discussion of this in the literature.

3.2.2 Mass resolution

We have examined the dependence of the density, velocity divergence, vorticity and vector potential on the mass resolution of the simulations. For the density and velocity divergence, there is evidence for a mild dependence on mass resolution for both of these fields on smaller scales. This is likely to be due to the DTFE window function, which cannot be compensated for, rather than a mass-resolution dependence of the field itself. There is no evidence of any mass-resolution dependence of these fields on larger scales. The variation of the density and velocity divergence with mass resolution can be seen in Figs 1 and 2 of file RB. The effect of the small-scale mass-resolution dependence is negligible for our HR simulations, as seen when comparing to alternative methods of calculating the density power spectrum.

The dependence of the vorticity power spectrum with mass resolution is shown in Fig. B1. The power spectrum shows spurious additional power when the mass resolution is insufficient. However, once the resolution is sufficient, of the order of $10^9\,\mathrm{M}_\odot$, there is no evidence for any systematic dependence on mass resolution. This dependence on mass resolution, followed by convergence around $\sim 10^9\,\mathrm{M}_\odot$, matches previous findings, notably those of Pueblas & Scoccimarro (2009).

In Fig. B2, we show the dependence of the vector potential on mass resolution. There is a clear dependence of the vector potential on mass resolution, similar to that seen for the vorticity. However, there are several differences. In particular, the mass-resolution
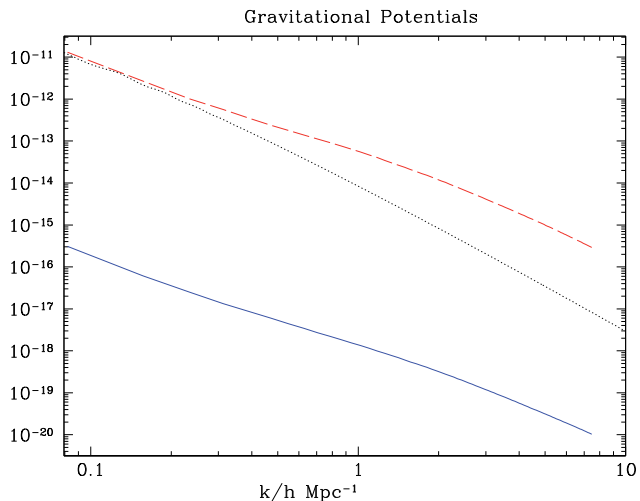
Figure 3. The scalar (dashed red line) and vector (solid blue line) gravitational potential power spectra at redshift zero, with the vector potential calculated using the curl method. The linear theory scalar potential is shown for comparison (dotted black line).
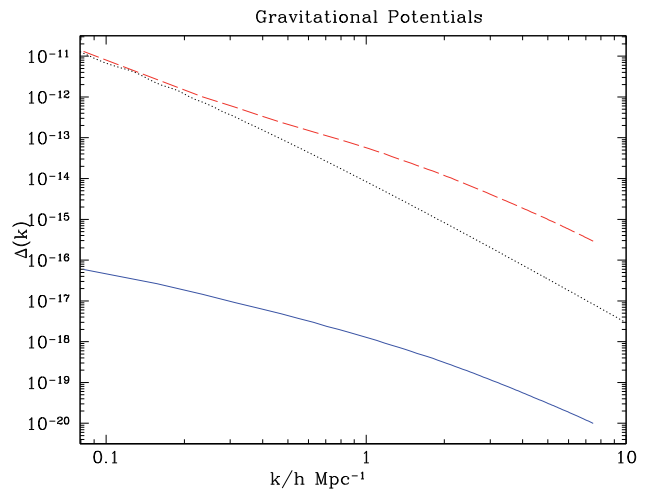

Figure 4. The scalar (dashed red line) and vector (solid blue line) gravitational potential power spectra at redshift zero, with the vector potential calculated using the momentum field method. The linear theory scalar potential is shown for comparison (dotted black line).

dependence seems to be less important for smaller scales, where there is a greater dependence on box size (see later). In addition, the dependence on mass resolution is still apparent around $10^9 \, \mathrm{M}_\odot$. However, once there mass resolution has improved to around $6 \times 10^8 \, \mathrm{M}_\odot$, there is no evidence of a mass-resolution dependence of the vector potential.

To show this further, Fig. B8 shows the higher resolution simulations in more detail, complete with the individual realizations of the HR simulations. The y-axis here is $k^2 P_B(k)$ in order to show the variance more clearly over the range of scales being considered. The cyan line shows the simulation with the worst resolution ($16.3 \times 10^8 \, \mathrm{M}_\odot$) of those in this plot and indeed this simulation shows a systematic deviation on the largest scales. The better resolution simulations show better convergence, with the $140 \, h^{-1}$ Mpc simulation with 768^3 particles being consistent with the HR simulations for essentially the entire range under consideration. This convergence is examined further in Appendix B4.

3.2.3 Box size

We have also considered the effect of varying the box size on the extracted power spectra. As expected, there is no evidence for any systematic dependence of the density, vorticity and velocity divergence power spectra on the box size of the simulations. This can be seen in Figs 3–5 of file RB. Note that, for sufficiently small boxes, a systematic deviation can arise, see Appendix B6.

Fig. B3 shows the box size dependence of the vector potential. As mentioned above, the vector potential does show some dependence on box size. The vector potential shows signs of a dependence on the box size on scales below $1 \, h^{-1}$ Mpc; however, this is difficult to entangle from the effects of mass resolution and the window function. For box sizes below $200 \, h^{-1}$ Mpc, there is no systematic dependence of the vector potential power spectrum with box size.

In Appendix B4, we examine the variation between realizations for the vector potential, and relate it to the behaviour that might be expected from perturbative arguments. In particular, Fig. B8 shows how the variation between realizations is larger than the effects of box size and mass resolution for simulations with box sizes below $200 \, h^{-1}$ Mpc and mass resolution of at least $6 \times 10^8 \, \mathrm{M}_\odot$. Thus,
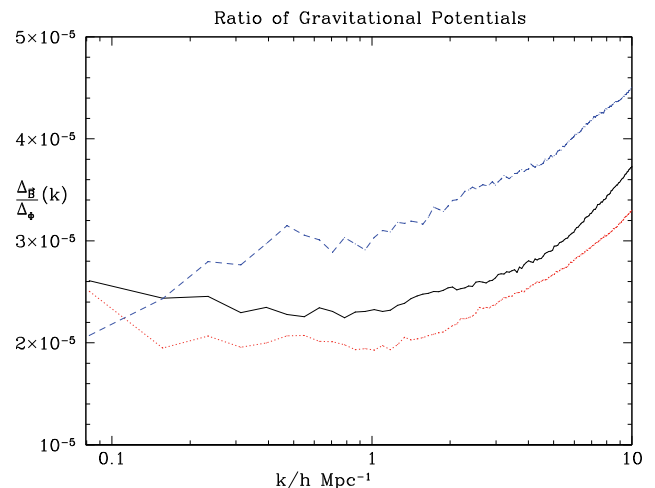
Figure 5. The ratio at redshift zero between the vector potential, calculated using the curl method, and the scalar potential. The three curves show the ratio for the three realizations of the HR simulations.

we expect numerical effects from the simulation parameters to be a sub-dominant source of error as long as the parameters are within this range.

3.2.4 Consistency checks

There are a few consistency checks that can be performed on the different fields that we are interested in. The quantities that are used for the vector potential include the density field and its gradients as well as the velocity field and its gradients. There are two relations between these fields and their derivatives,

$$k^2 P_\delta(k) = P_{\nabla\delta}(k) \tag{12}$$

$$k^2 P_v(k) = P_{\nabla \cdot v}(k) + P_{\nabla \times v}(k). \tag{13}$$

We have extracted the quantities on the left- and right-hand sides of these relations from our HR simulations and compared them; see Fig. 1 in file CC for the ratio $P_{\nabla\delta}(k)/k^2 P_\delta(k)$ and Fig. 2 in file CC for

the ratio $k^2 P_v(k)/(P_{\nabla \cdot v}(k) + P_{\nabla \times v}(k))$. In both cases, two curves are plotted, corresponding to two different methods of calculating the ratio. The blue line shows the ratio exactly as suggested above, with the factor of k in equation (12) taken to be the value defining the centre of the bin. For the red curve, the exact k-value for each mode is used when computing the sum in each bin. For small bins, or fields where the values vary slowly as a function of k, these two should agree and indeed they do for smaller scales where our (logarithmic) bins are smaller. There is a difference between the methods for the largest scales in our simulations; this will be discussed below for each test.

For the density field, the two methods for calculating the ratio do give different answers. However, for both methods, the deviation is within 2 per cent for every bin except the first. Thus, this consistency check for the density field is well satisfied for all scales $k \geq 0.2\,h\,\mathrm{Mpc}^{-1}$.

The consistency check for the velocity field is less well satisfied: there is a sharp divergence in the power spectra on the smallest scales, such that the check is not satisfied within 10 per cent at $k \approx 8\,h^{-1}$ Mpc. This shows the effect of the DTFE window function on the extracted fields. We will not consider the extracted vector potential for k larger than $k \approx 8\,h^{-1}$ Mpc when presenting our results. Furthermore, the two methods show very different behaviour: the method using the average k-value for each bin causes the consistency test to fail on large scales. However, with the more exact method, the consistency check is very well satisfied on all of the largest scales. This suggests that the dominant contribution to the bins on the largest scales comes from the low-k end of each bin, hence the overestimation of $k^2 P_v(k)$ when the average k-value for each bin is used. The strong effect here is partly caused by the relatively steep slope of the velocity power spectrum. We note that this effect would also come into play when calculating the dimensionless velocity power spectrum for binned data. None the less, the good agreement of the consistency check when using the second method is strong evidence that the derivatives of the velocity field are being calculated correctly.

A further check that we can perform is to extract the complete momentum field, $\boldsymbol{p} = (1 + \delta)\boldsymbol{v}$, and decompose it into its vector and scalar parts directly rather than dealing with derivatives. The power spectrum of the vector potential can then be calculated from the vector part of the momentum field, $\boldsymbol{p}^v$, using

$$P_{B^N}(k) = \left(\frac{16\pi G \rho_b a^2}{k^2} \right)^2 P_{p^v}(k). \tag{14}$$

In Fig. 1 we show the ratio of the vector power spectrum calculated using the two methods, with the different lines corresponding to different individual realizations. The vector potentials calculated from the two methods are broadly consistent, within 20 per cent for most of the range under consideration, and agreeing to within a factor of 2 for $k \geq 0.2\,h\,\mathrm{Mpc}^{-1}$. We are unsure what the causes of the difference between the two methods are. In particular, we checked for whether there is an effect coming from the use of k averaged over the bin, as in the velocity field consistency check; however, this effect is negligible for the gravitomagnetic potential.[1]

The difference between the methods is larger than the variation amongst realizations for either method.

We can also extract the momentum field directly using a standard CiC approach (Hockney & Eastwood 1981), and compare this to the momentum field extracted using the DTFE code. The ratio between these fields is shown in Fig. 2. There is good agreement between the two methods of computing the momentum power spectrum on larger scales, but with a divergence between the two methods on smaller scales. It is unclear which method would be expected to be more accurate on these smaller scales: the DTFE method suffers from having a window function that cannot be deconvolved; however, the CiC method will have cells with a zero momentum field, due to the lack of nearby particles, for a sufficiently large grid. In fact, the CiC method does not converge as the grid size is increased. We used a 512^3 grid for the CiC code, although we checked that changing this to 256 or 1024 does not significantly affect the results. Unlike the DTFE method, derivatives cannot be directly extracted with the CiC method, so the consistency checks performed earlier for the DTFE method cannot be applied to the CiC method. This also means that the first method of extracting the vector potential, using the curl of the momentum field, cannot be carried out with the CiC method.

We present the vector power spectrum from both the momentum field and the curl method in the results section. We note that the level of agreement between Figs 1 and 2 suggests that our vector potential power spectrum is robust and correct to within a factor of 2. It is unclear to us which method should be trusted more; whilst the momentum field method is simpler, the derivative method allows us to examine the different components, notably the vorticity, and check that it behaves as expected. The differences between the two methods do not affect the observability of the vector potential; see Bruni et al. (2014) and Thomas et al. (2014).

3.2.5 Comparison to previous findings

There are several works in the literature to which we can compare our findings on the velocity field and its components. As mentioned above, the vorticity and velocity divergence power spectra were extracted from *N*-body simulations in Pueblas & Scoccimarro (2009) using an alternative implementation of the Delaunay tessellation. They found a strong dependence on resolution of the extracted vorticity power spectrum and an approximate scaling of the vorticity power spectrum with the seventh power of the linear growth factor.

The vorticity and velocity divergence power spectra in Pueblas & Scoccimarro (2009) are consistent with the spectra extracted for this paper and we found the same resolution dependence of the vorticity power spectrum (see above). However, as detailed in Appendix B2, we do not find the same scaling of the vorticity spectrum with the seventh power of the linear growth factor (D_+). Although this scaling seems to hold at low redshift, it no longer holds at redshift one and beyond. At these earlier times, the power spectrum is smaller than expected from the growth factor to the seventh scaling, so the vorticity power spectrum must have grown by less at redshift two than expected.

Two recent publications (Koda et al. 2014; Zheng et al. 2013) have examined the velocity field from the point of view of redshift space distortions. In these works, a different method of extracting velocity fields is used, the nearest particle method. In this method, the velocity at a grid point is given by the velocity of the nearest

---

[1] As an aside, we note that we also calculated the momentum field by extracting the velocity field and density field separately at each grid point, before multiplying them together. The power spectrum calculated from this field agrees well with that calculated by extracting the momentum field as a single field. The same agreement is not obtained when extracting the field

δ^2 and comparing to squaring the density field, when using either the DTFE code or a CiC method.

particle to that grid point. See those works for comments on the differences between the nearest particle and Delaunay tessellation methods of extracting the velocity power spectra. Here, we note that there appear to be pros and cons to both methods, with no clear 'better' method. It would be interesting to examine how close the agreement between the vector potentials extracted by the DTFE and nearest particle methods is.

None the less, there are some general observations that can be compared between these works. Notably, the magnitude of the velocity and vorticity spectra is found to be similar, considering the differences in cosmological parameters. Also, the onset of non-linearity is found to occur at lower k for the velocity divergence than for the density. In addition, Zheng et al. (2013) find a strong dependence of the curl component of the velocity field on the resolution, similarly to both this paper and Pueblas & Scoccimarro (2009). They also find a time dependence of this component that is approximately D_+^7 up to $z = 2$, although this relationship breaks down by up to a factor of 2 for certain redshifts and scales. As mentioned above, whilst our simulations also find this time dependence of the vorticity at low redshift, we find that the relationship breaks down for $z > 1$. There is no examination of multiple realizations in Zheng et al. (2013) and, similarly to the comments in Appendix B2 regarding Pueblas & Scoccimarro (2009), the difference between our realizations is sufficient to explain the difference between our results and those of Zheng et al. (2013).

The broad agreement between different methods, including agreement regarding resolution dependence and convergence, is promising. Details of the vorticity field and its evolution require further study, but the vorticity is a sub-dominant contribution to the vector potential. As the simulations and snapshots used in the papers mentioned in this section are different from ours, it is not possible to compare the methods and extracted fields any more precisely. We note that the three works mentioned here do not have multiple realizations of their HR simulations, so we are unable to determine if the variation in vorticity between realizations found by us is reproduced (see Appendix B4).

As this paper was being prepared, Hahn, Angulo & Abel (2014) appeared on the arXiv. This paper investigates the properties of velocity divergence and vorticity and confirms many of the findings of Pueblas & Scoccimarro (2009). In particular, they agree with our results regarding the convergence of the DTFE code for sufficient mass resolution and our finding of a resolution dependence of the velocity divergence, which did not appear in Pueblas & Scoccimarro (2009). They use a different method to compute the vorticity and velocity divergence power spectra, which agrees with the DTFE code for sufficient resolution. However, as with the previous papers, there seems to be no examination of multiple realizations with the same resolution, in order to compare our findings. In addition, there is no examination of the time dependence and thus no confirmation or rejection of the D_+^7 scaling of the vorticity spectrum at higher redshifts.

4 RESULTS

In this section, we present the power spectrum of the post-Friedmann vector potential as calculated from N-body simulations. We show the power spectrum at $z = 0$ and the different components of the source, as well as the evolution of the power spectrum between $z = 2$ and 0. In addition, we show the ratio between the vector and scalar power spectra, and examine the time evolution of this quantity as well. The power spectra plotted for the scalar and vector gravitational potentials are the dimensionless power spectra. The closest analytic

result to our calculation is the second-order perturbative vector potential calculated in Hui-Ching Lu et al. (2009). We will compare our results to theirs at redshift $z = 0$, as well as comparing the time evolution.

4.1 Results at redshift zero

In Figs 3 and 4, we show the power spectrum of the post-Friedmann vector potential as well as the standard Newtonian scalar potential, at $z = 0$, for the curl and momentum field methods of extraction, respectively. As expected, both methods show that the scalar potential is small over all scales and the vector potential is sub-dominant. There is a quantitative difference between the two methods on the largest scales, but this difference is not sufficient to alter the expected qualitative behaviour. Notably, the effect of the vector potential on weak-lensing power spectra, as examined in Thomas et al. (2014), will remain negligible, regardless of which method is used to calculate the vector potential. We have been unable to determine the reason for this discrepancy and it is unclear to us which method should, a priori, be expected to be more accurate.

In Figs 5 and 6, we show the ratio between the power spectra of the vector and scalar gravitational potentials at redshift zero, for the two methods of extracting the vector potential. We plot the ratios for all three individual realizations of the HR simulations. For the curl method, as shown in Bruni et al. (2014), this ratio is approximately 2.5×10^{-5}. This ratio does not vary significantly over the range of scales considered, although there is a slight increase towards smaller scales. However, for the momentum field method, the ratio is not approximately constant due to the decreased power on large scales. We will compare this behaviour to the analytic second-order perturbative behaviour shortly; here we just note that the curl method produces qualitative behaviour that is closer to the analytic prediction.

In Fig. 7, we show the power spectra of the three sources of the vector potential using the curl method, see equation (8). The power spectra plotted here are given by $P(k)/\left(f^2\mathcal{H}^2(2\pi)^3\right)$, where $\mathcal{H}$ is the conformal time Hubble constant and $f = \mathrm{d}\ln D/\mathrm{d}\ln a$ is the logarithmic derivative of the linear growth factor D. These units are chosen such that the power spectrum of the velocity divergence agrees with the density power spectrum on linear scales and have the same units as the matter power spectrum, following Pueblas
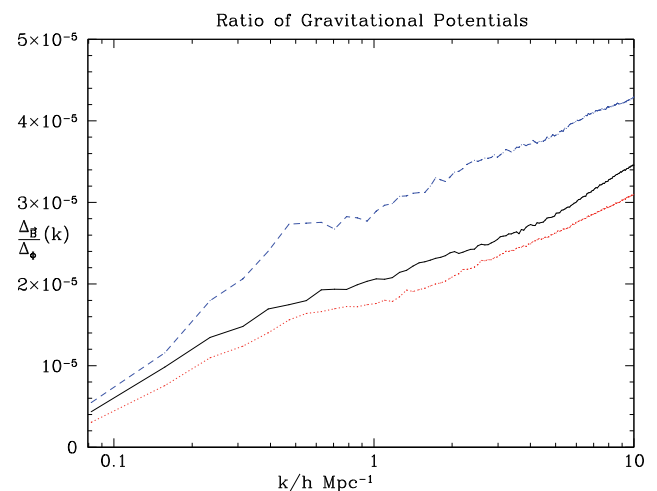

Figure 6. The ratio at redshift zero between the vector potential, calculated using the momentum field method, and the scalar potential. The three curves show the ratio for the three realizations of the HR simulations.
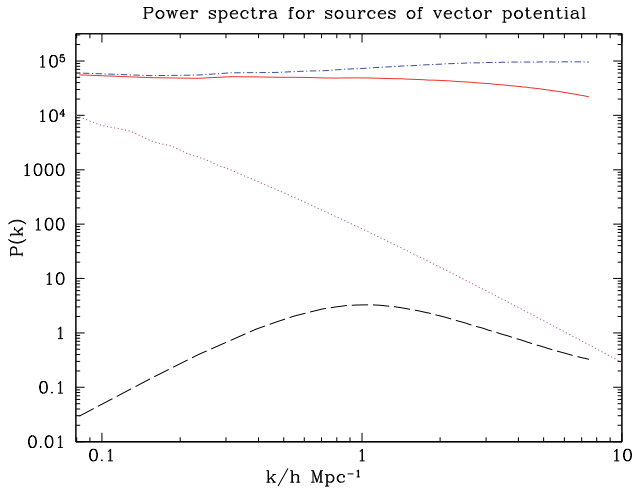
Power spectra for sources of vector potential

Figure 7. The power spectra of the three source terms for the vector potential in equation (8), the vorticity (dashed black line), $\nabla\delta \times \boldsymbol{v}$ (dot–dashed blue line) and $\delta\nabla \times \boldsymbol{v}$ (solid red line). The power spectra plotted here are given by $P(k)/\left(f^2\mathcal{H}^2(2\pi)^3\right)$, such that the power spectrum of the velocity divergence agrees with the density power spectrum on linear scales and ensuring that all of the power spectra have the same units, following Pueblas & Scoccimarro (2009). The linear matter power spectrum is shown as a dotted magenta line for comparison.

& Scoccimarro (2009). The vorticity, although often ignored in perturbation theory, is the only one of these three quantities that is linear in perturbations. This figure shows that it is negligible compared to the other two components, so the vector potential is being predominantly generated by non-linear effects.

Since this vector potential is the first correction to Newtonian theory, this calculation is the first quantitative check of the relationship between Newtonian simulations and GR on fully non-linear scales. The small magnitude of the vector potential suggests that running Newtonian simulations is sufficiently accurate for cosmological purposes, whereas a larger calculated value for the vector potential would suggest that the approximations taken in deriving the fully non-linear Newtonian equations do not hold sufficiently well. As far as relating Newtonian and relativistic cosmologies goes, in the language of Green & Wald (2012), the smallness of this vector potential allows the use of the abridged dictionary in Chisari & Zaldarriaga (2011), rather than the dictionary proposed in Green & Wald (2012). We note that the analysis here is for a ΛCDM cosmology; further work is required to determine the validity of Newtonian simulations in general dark energy cosmologies.

4.2 Time evolution

In this section, we will examine the time evolution of the vector potential, and its ratio to the scalar potential, for the redshifts listed in Table 2. The vector potential is this section has been computed using the curl method. In Fig. 8, we plot the ratio of the vector potential to the scalar potential as a function of redshift. The different curves in this plot show the evolution for different wavenumbers. We can see that individual k modes do not exhibit significant growth over time, although the more non-linear scales do exhibit slightly more variation in time. Similarly to the scalar gravitational potential, the vector potential at a fixed scale is not monotonic over time on non-linear scales.

In Fig. 9, we plot the ratio of the vector potential to the scalar potential as a function of redshift. The different curves in this plot

Table 2. Redshifts used to probe time evolution of quantities.

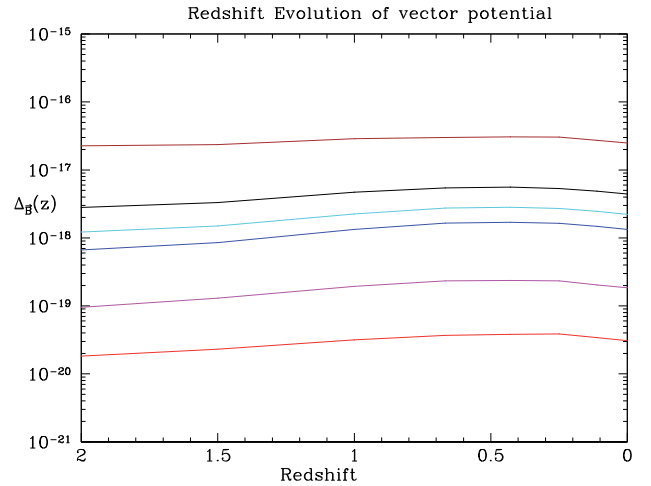| Scale factor	Redshift	Colour on time evolution plots
0.33	2.0	Black
0.4	1.5	Red
0.5	1.0	Magenta
0.6	0.67	Yellow
0.7	0.43	Green
0.8	0.25	Cyan
0.9	0.11	Blue
1.0	0.0	Brown

Figure 8. The evolution of the vector potential for six different wavenumbers. From top to bottom, these are $k = 0.23\,h\,\mathrm{Mpc}^{-1}$ (brown), $k = 0.55\,h\,\mathrm{Mpc}^{-1}$ (black), $k = 0.79\,h\,\mathrm{Mpc}^{-1}$ (cyan), $k = 1.01\,h\,\mathrm{Mpc}^{-1}$ (blue), $k = 2.51\,h\,\mathrm{Mpc}^{-1}$ (magenta) and $k = 5.03\,h\,\mathrm{Mpc}^{-1}$ (red).
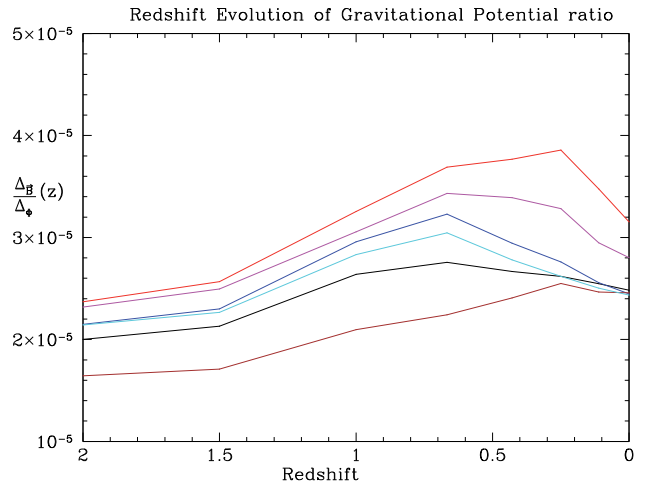

Figure 9. The ratio of the vector potential to the scalar potential plotted for six different wavenumbers. From bottom to top (at redshift = 1), these are $k = 0.23\,h\,\mathrm{Mpc}^{-1}$ (brown), $k = 0.55\,h\,\mathrm{Mpc}^{-1}$ (black), $k = 0.79\,h\,\mathrm{Mpc}^{-1}$ (cyan), $k = 1.01\,h\,\mathrm{Mpc}^{-1}$ (blue), $k = 2.51\,h\,\mathrm{Mpc}^{-1}$ (magenta) and $k = 5.03\,h\,\mathrm{Mpc}^{-1}$ (red).

show the same wavenumbers as in Fig. 8. The ratio stays fairly constant over time, varying by less than a factor of 2 for a given scale. Across the entire range of times and scales under consideration, the ratio varies by less than a factor of 4. The ratio between the

gravitational potentials is also not monotonic over the redshift range under consideration for a given scale.

4.2.1 Comparison to perturbative calculation

In Hui-Ching Lu et al. (2009), an analytic calculation of the vector potential was performed using perturbation theory. As a perturbative analysis, it is unclear how large a value of k this calculation should be extended to. Here we will assume that it is valid on all of the scales of overlap between this method and ours.

For the curl method of computing the vector power spectrum, there is similar qualitative behaviour between the two methods, with the ratio of the power spectra of the vector and scalar potentials being fairly constant and of the order of 10^{-5} in both methods. The difference between the two methods being that the ratio in Hui-Ching Lu et al. (2009) is between the vector and the linear theory scalar potential, whereas the our ratio is between the vector and the fully non-linear scalar potential. This means that despite this similar qualitative behaviour, the power spectrum of the vector potential in Hui-Ching Lu et al. (2009) underestimates the fully non-linear value on these scales by up to two orders of magnitude, the same factor by which the linear theory scalar potential power spectrum underestimates the power spectrum of the fully non-linear scalar potential.

The momentum field method of calculating the vector power spectrum results in less similar qualitative behaviour. It is unclear how well the gravitomagnetic potential would be expected to match the perturbative prediction on these scales as the velocity field differs from the linear theory at larger scales than the density.

The power spectrum of the perturbative vector potential is given in Hui-Ching Lu et al. (2009) as

$$\mathcal{P}_s(k) = \left(\frac{2\Delta_{\mathcal{R}}}{5g_\infty}\right)^4 \left(\frac{3g\left[g' + \mathcal{H}\right]}{\Omega_m \mathcal{H}^2}\right)^2 k^2 \Pi(u^2), \tag{15}$$

where $\mathcal{P}_s$ is the dimensionless power spectrum of the vector potential, $\Delta_{\mathcal{R}}$ is the primordial power of the curvature perturbation, g is the growth factor for the scalar potential, g_∞ is a normalization parameter chosen so $g(0) = 1$, Π is a function of the transfer function, Ω_m is the time-dependent matter density and $\mathcal{H}$ is the conformal Hubble constant. The second term in parentheses contains all of the time dependence of the vector potential power spectrum and essentially acts as the growth factor for the vector potential. We have compared this perturbative prediction for the growth factor of the vector potential to the growth measured in the simulations (see Fig. 5 in file CC). This shows that the analytic prediction is not the main source of the time evolution of the vector potential.

5 CONCLUSION AND DISCUSSION

In this paper, we have presented the post-Friedmann frame-dragging vector potential calculated on non-linear scales from N-body simulations. We have presented this vector potential at redshift zero, as well as examining its evolution with redshift. We have also presented the tests we have performed in order to establish the robustness of our result, including tests of simulation parameters and different methods of extracting the source of the vector potential.

We have shown that our density, velocity divergence and vorticity spectra are consistent with the literature and show similar behaviour regarding convergence tests, particularly mass resolution. We do not see the vorticity scaling with the seventh power of the linear growth factor D_+ (Pueblas & Scoccimarro 2009) beyond $z = 1$; however,

the differences between our results and others' are within the variance between realizations. We have noted a larger variation of the vorticity than the density and velocity divergence fields between different realizations, a result that does not seem to have been studied in the literature.

We have shown that there is no evidence for a systematic dependence of the vector potential spectrum on box size for boxes smaller than 200 h^{-1} Mpc or on mass resolution with mass resolution better than $6 \times 10^8 M_\odot$. There is also no evidence that the vector potential is sensitive to the softening length, binning, number of samples (an internal DTFE parameter) or the grid size used in the analysis. There is reasonable agreement between the different methods (curl and momentum field) of extracting the vector potential, although there is an unresolved discrepancy between the two methods on the largest scales. We do however note the importance of the variation of the vector potential between realizations; this issue is discussed more fully in Appendix B4.

Figs 3 and 8 comprise the main physical results of this paper, showing the magnitude of the vector potential power spectrum at redshift zero and its evolution with time, respectively. The magnitude of the vector potential power spectrum can also be expressed in terms of its ratio to the power spectrum of the scalar potential, as shown in Figs 5 and 9. We have shown that the power spectrum of the vector potential is around 10^5 times smaller than the power spectrum of the scalar potential, over a range of scales and redshifts. These values were used in Bruni et al. (2014) and Thomas et al. (2014) when examining the observability of the vector potential, showing that it is negligible for currently planned weak-lensing surveys. The small magnitude of the vector potential found here is the first quantitative check of the validity of Newtonian simulations compared to GR on fully non-linear scales and supports the use of Newtonian simulations for computing cosmological observables. In terms of interpreting the simulations, the small value of this vector potential seems to justify the use of the abridged dictionary in Chisari & Zaldarriaga (2011), rather than the dictionary proposed in Green & Wald (2012), for relating GR and Newtonian cosmologies.

The work carried out so far considers a ΛCDM cosmology, so this conclusion may no longer be true for a dark energy or modified gravity cosmology. The post-Friedmann approach would need to be expanded to include modified Einstein equations and/or a fluid with pressure in order to examine alternative cosmologies and determine whether the use of Newtonian-type N-body simulations is still valid in those cosmologies. The post-Friedmann expansion has been applied to $f(R)$ gravity and the vector potential calculated from $f(R)$ simulations in Thomas et al. (2015). The vector potential in $f(R)$ was found to be larger than that in GR. We hope that this, and further extensions to the work in this paper, will allow us to understand how generic the findings in this paper are, and thus justify one of the most widely used tools in cosmology, N-body simulations. Whilst this paper was being prepared for submission, Adamek, Durrer & Kunz (2014) appeared on the arXiv. Their preliminary results seem to agree with the results of this work. It will be interesting to perform a more in-depth comparison once the details of their work are available.

(HPC) cluster which is supported by the Institute of Cosmology and Gravitation (ICG) and the University of Portsmouth. The rest were undertaken on the COSMOS Shared Memory system at DAMTP, University of Cambridge operated on behalf of the STFC DiRAC HPC Facility. This equipment is funded by BIS National E-infrastructure capital grant ST/J005673/1 and STFC grants ST/H008586/1, ST/K00333X/1. This work was supported by STFC grants ST/H002774/1, ST/L005573/1 and ST/K00090X/1.

REFERENCES

Adamek J., Daverio D., Durrer R., Kunz M., 2013, Phys. Rev. D, 88, 103527
Adamek J., Durrer R., Kunz M., 2014, Class. Quantum Grav., 31, 234006
Bagla J. S., Prasad J., 2006, MNRAS, 370, 993
Bagla J. S., Ray S., 2005, MNRAS, 358, 1076
Bernardeau F., van de Weygaert R., 1996, MNRAS, 279, 693
Bruni M., Thomas D. B., Wands D., 2014, Phys. Rev. D, 89, 044010
Carbone C., Matarrese S., 2005, Phys. Rev. D, 71, 043508
Cautun M. C., van de Weygaert R., 2011, preprint (arXiv:1105.0370)
Chandrasekhar S., 1965, ApJ, 142, 1488
Chisari N. E., Zaldarriaga M., 2011, Phys. Rev. D, 83, 123505
Colombi S., Jaffe A., Novikov D., Pichon C., 2009, MNRAS, 393, 511
Crocce M., Pueblas S., Scoccimarro R., 2006, MNRAS, 373, 369
Everitt C. W. F. et al., 2011, Phys. Rev. Lett., 106, 221101
Flender S. F., Schwarz D. J., 2012, Phys. Rev. D, 86, 063527
Gelb J. M., Bertschinger E., 1994, ApJ, 436, 491
Green S. R., Wald R. M., 2012, Phys. Rev. D, 85, 063512
Hahn O., Angulo R. E., Abel T., 2014, preprint (arXiv:1404.2280)
Haugg T., Hofmann S., Kopp M., 2012, preprint (arXiv:1211.0011)
Hockney R. W., Eastwood J. W., 1981, Computer Simulation Using Particles. McGraw-Hill, New York
Hui-Ching Lu T., Ananda K., Clarkson C., Maartens R., 2009, J. Cosmol. Astropart. Phys., 2, 23
Hwang J.-c., Noh H., 2013, J. Cosmol. Astropart. Phys., 4, 35
Hwang J.-c., Noh H., Puetzfeld D., 2008, J. Cosmol. Astropart. Phys., 3, 10
Koda J. et al., 2014, MNRAS, 445, 4267
Kopp M., Uhlemann C., Haugg T., 2014, J. Cosmol. Astropart. Phys., 3, 18
Lu T. H.-C., Ananda K., Clarkson C., 2008, Phys. Rev. D, 77, 043523
Matarrese S., Terranova D., 1996, MNRAS, 283, 400
Milillo I., 2010, PhD thesis, University of Portsmouth
Milillo I., Bertacca D., Bruni M., Maselli A., 2015, preprint (arXiv:1502.02985)
Poisson E., Will C. M., 2014, Gravity: Newtonian, Post-Newtonian, Relativistic. Cambridge Univ. Press, Cambridge
Pueblas S., Scoccimarro R., 2009, Phys. Rev. D, 80, 043504
Schaap W. E., van de Weygaert R., 2000, A&A, 363, L29
Shibata M., Asada H., 1995, Prog. Theor. Phys., 94, 11
Springel V., 2005, MNRAS, 364, 1105
Takada M., Futamase T., 1997, preprint (arXiv:astro-ph/9711344)
Thomas D. B., Bruni M., Wands D., 2014, preprint (arXiv:1403.4947)
Thomas D. B., Bruni M., Koyama K., Li B., Zhao G.-B., 2015, preprint (arXiv:1503.07204)
Tomita K., 1991, Prog. Theor. Phys., 85, 1041
van de Weygaert R., Schaap W., 2009, in Martínez V. J., Saar E., Martínez-González E., Pons-Bordería M.-J., eds, Lecture Notes in Physics, Vol. 665, Data Analysis in Cosmology. Springer-Verlag, Berlin, p. 291
Weinberg S., 1972, Gravitation and Cosmology: Principles and Applications of the General Theory of Relativity. Wiley, New York
Zheng Y., Zhang P., Jing Y., Lin W., Pan J., 2013, Phys. Rev. D, 88, 103510

SUPPORTING INFORMATION

Additional Supporting Information may be found in the online version of this article:

Resolution_and_BoxSize_Dependence.pdf
GridSize_and_Binning_Dependence.pdf
ConsistencyChecks.pdf
(http://mnras.oxfordjournals.org/lookup/suppl/doi:10.1093/mnras/stv1390/-/DC1).

Please note: Oxford University Press are not responsible for the content or functionality of any supporting materials supplied by the authors. Any queries (other than missing material) should be directed to the corresponding author for the paper.

APPENDIX A: VECTOR POWER SPECTRA

We will be dealing with vector quantities, for which there are different ways to define the power spectrum. Our power spectrum for a generic vector $\boldsymbol{v}$ is defined as

$$\langle \tilde{\boldsymbol{v}}(\boldsymbol{k}) \cdot \tilde{\boldsymbol{v}}^*(\boldsymbol{k}') \rangle = (2\pi)^3 \delta^3(\boldsymbol{k} - \boldsymbol{k}') P_v(k). \tag{A1}$$

Note that for a divergenceless vector, such as $\boldsymbol{B}^{\mathrm{N}}$, $k^2 P_{\boldsymbol{B}^{\mathrm{N}}}(k) = P_{\nabla \times \boldsymbol{B}^{\mathrm{N}}}(k)$. With our Fourier transform convention, the dimensionless power spectrum for a field X is given by $\Delta_X = k^3 P_X(k)/2\pi^2$. All plots of the power spectrum of the vector potential show the dimensionless power spectrum.

Using equation (7)

$$\left\langle \widetilde{\nabla \times \boldsymbol{B}^{\mathrm{N}}}(\boldsymbol{k}) \cdot \widetilde{\nabla \times \boldsymbol{B}^{\mathrm{N}*}}(\boldsymbol{k}') \right\rangle = \left(\frac{16\pi G \rho_b a^2}{k^2} \right)^2 \left\langle \left[\widetilde{(\nabla \delta) \times \boldsymbol{v}} + \widetilde{(1+\delta)\nabla \times \boldsymbol{v}} \right] \cdot \left[\widetilde{(\nabla \delta) \times \boldsymbol{v}} + \widetilde{(1+\delta)\nabla \times \boldsymbol{v}} \right]^* \right\rangle \tag{A2}$$

$$\langle \widetilde{\nabla \times \boldsymbol{B}^{\mathrm{N}}}(\boldsymbol{k}) \cdot \widetilde{\nabla \times \boldsymbol{B}^{\mathrm{N}*}}(\boldsymbol{k}') \rangle = \left(\frac{16\pi G \rho_b a^2}{k^2} \right)^2 \begin{pmatrix} \langle [\widetilde{\nabla \delta \times \boldsymbol{v}}] \cdot [\widetilde{\nabla \delta \times \boldsymbol{v}}]^* \rangle & +\langle [\widetilde{\nabla \delta \times \boldsymbol{v}}] \cdot [\widetilde{\delta \nabla \times \boldsymbol{v}}]^* \rangle & +\langle [\widetilde{\nabla \delta \times \boldsymbol{v}}] \cdot [\widetilde{\nabla \times \boldsymbol{v}}]^* \rangle \\ +\langle [\widetilde{\delta \nabla \times \boldsymbol{v}}] \cdot [\widetilde{\nabla \delta \times \boldsymbol{v}}]^* \rangle & +\langle [\widetilde{\delta \nabla \times \boldsymbol{v}}] \cdot [\widetilde{\delta \nabla \times \boldsymbol{v}}]^* \rangle & +\langle [\widetilde{\delta \nabla \times \boldsymbol{v}}] \cdot [\widetilde{\nabla \times \boldsymbol{v}}]^* \rangle \\ +\langle [\widetilde{\nabla \times \boldsymbol{v}}] \cdot [\widetilde{\nabla \delta \times \boldsymbol{v}}]^* \rangle & +\langle [\widetilde{\nabla \times \boldsymbol{v}}] \cdot [\widetilde{\delta \nabla \times \boldsymbol{v}}]^* \rangle & +\langle [\widetilde{\nabla \times \boldsymbol{v}}] \cdot [\widetilde{\nabla \times \boldsymbol{v}}]^* \rangle \end{pmatrix} \cdot$$

Noting that $A \cdot B^* = (A^* \cdot B)^*$,

$$\langle [\widetilde{\nabla \times \boldsymbol{v}}] \cdot [\widetilde{\nabla \delta \times \boldsymbol{v}}]^* \rangle + \langle [\widetilde{\nabla \delta \times \boldsymbol{v}}] \cdot [\widetilde{\nabla \times \boldsymbol{v}}]^* \rangle = 2\mathrm{re} \left(\langle (\widetilde{\nabla \times \boldsymbol{v}}) \cdot (\widetilde{\nabla \delta \times \boldsymbol{v}}) \rangle \right) \equiv (2\pi)^3 \delta^3(\boldsymbol{k} - \boldsymbol{k}') P_{(\nabla \delta \times \boldsymbol{v})(\nabla \times \boldsymbol{v})}(k). \tag{A3}$$

And therefore the dimensionless power spectrum for the vector potential is given by

$$\Delta_{B^{\mathrm{N}}}(k) = \left(\frac{16\pi G \rho_b a^2}{k^2} \right)^2 \frac{k}{2\pi^2} P_{\delta v}(k),$$ (A4)

where

$$P_{\delta v}(k) = P_{\nabla \times v}(k) + P_{\delta \nabla \times v}(k) + P_{(\nabla \delta) \times v}(k) + P_{(\nabla \delta \times v)(\nabla \times v)}(k) + P_{(\nabla \delta \times v)(\delta \nabla \times v)}(k) + P_{(\delta \nabla \times v)(\nabla \times v)}(k).$$ (A5)

APPENDIX B: ADDITIONAL ROBUSTNESS INFORMATION

In this appendix, we show the figures referred to in the main text (Figs B1–B3) as well as discussing additional robustness and convergence tests that were carried out in order to establish our result.

B1 DTFE parameters

There are several internal DTFE parameters that are used when computing these fields on a regular grid. We investigate the effects of two of these parameters here, the grid size and the number of samples that are made in each grid cell, N_{samples}.

We examined the effect of varying the grid size on the extracted density, velocity divergence and vorticity power spectra. In all cases, the agreement is very good, except on the smallest scales. A discrepancy on this scales is expected due to the change in the resolution of the grid and the effects of the DTFE window function. However, even on the smallest scales, the discrepancy is small. This can be seen in Figs 1–3 in
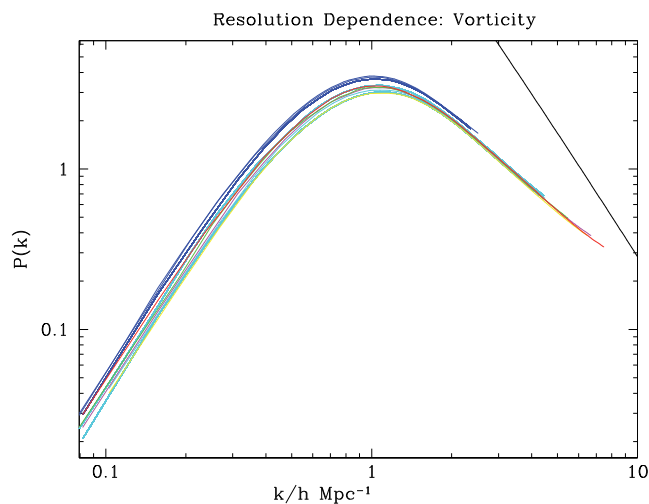

Figure B1. The vorticity power spectra extracted from simulations with varying box size and mass resolution. Lines with the same colour share the same mass resolution [in units of 10^8 M$_\odot$: 3.97 (red), 6.26 (magenta), 6.31 (yellow), 7.76 (green), 16.3 (cyan) and 130 (blue)]. The black curve is the linear matter power spectrum for comparison.
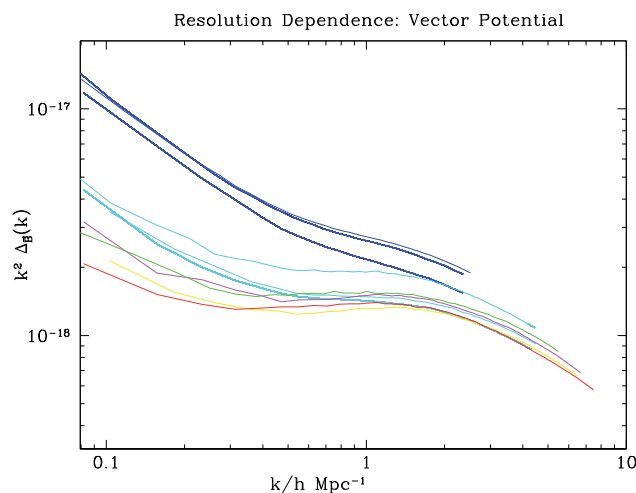

Figure B2. The vector potential power spectra extracted from simulations with varying box size and mass resolution. Lines with the same colour share the same mass resolution [in units of 10^8 M$_\odot$: 3.97 (red), 6.26 (magenta), 6.31 (yellow), 7.76 (green), 16.3 (cyan) and 130 (blue)]. The spectra have been multiplied by k^2 in order to better show the variation.
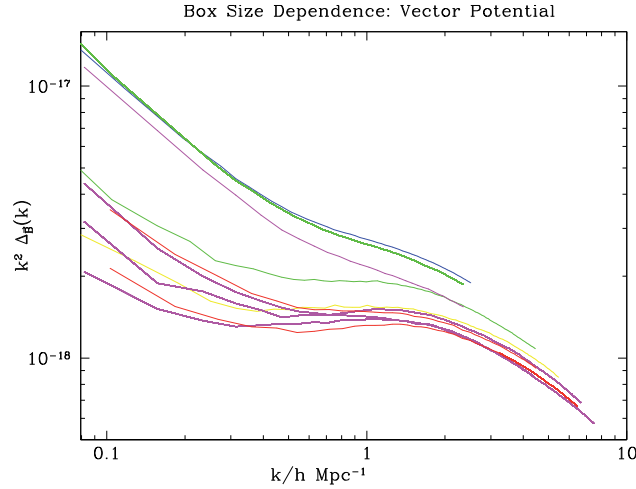
Figure B3. The vector potential power spectra extracted from simulations with varying box size and mass resolution. Lines with the same colour share the same box size: 140 h^{-1} Mpc (red), 160 h^{-1} Mpc (magenta), 200 h^{-1} Mpc (yellow), 240 h^{-1} Mpc (green), 320 h^{-1} Mpc (blue). The spectra have been multiplied by k^2 in order to better show the variation.
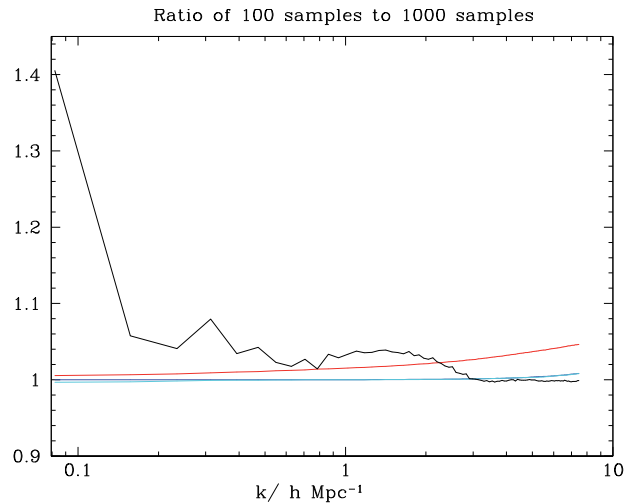

Figure B4. The ratios of the power spectra computed with $N_{\mathrm{samples}} = 100$ and 1000. The ratios shown are for the density (red), velocity divergence (blue), vorticity (cyan) and vector potential (black).

file BG, where we show the extracted spectra from one of the 160 h^{-1} Mpc simulations with 1024^3 particles at redshift zero. The different lines show the different grid sizes used: 1024 (blue), 950 (cyan), 850 (green), 750 (magenta) and 640 (red). The black line shows the linear density power spectrum for comparison. For our result plots, we have used the suggested value $N_{\mathrm{grid}}^3 = N_{\mathrm{part}} = 1024$.

Our analysis has all been carried out with $N_{\mathrm{samples}} = 100$ points per grid cell, partly due to computing constraints; increasing the number of samples increases the run time and memory required when analysing a snapshot. However, in Fig. B4 we show the effect of increasing N_{samples} to 1000 points per grid cell for one of the 160 h^{-1} Mpc simulations with 1024^3 particles. The velocity divergence and vorticity spectra agree very well between the two different numbers of samples. The density power spectrum shows a deviation that increases towards smaller scales, however is within 5 per cent for the range of scales under consideration here. The power spectrum of the vector potential shows more deviation, with decreasing deviation for smaller scales. However, the change in the vector potential is within 10 per cent for every bin after the first and is within 5 per cent for all scales $k > 0.3\,h^{-1}$ Mpc.

B2 Linear evolution

A further check that can be performed is to examine how the time variation of our extracted density, velocity divergence and vorticity power spectra compares to the respective linear predictions. For the density and velocity divergence fields, the power spectra evolve as $(D_+(z)/D_+(z = 0))^2$ on the largest scales and earliest times, as per the linear theory prediction. This prediction becomes increasingly inaccurate for more scales at lower redshifts due to non-linear effects.

The time evolution that we found for the vorticity is shown in Fig. B5. In this figure, the power spectrum at each redshift has been divided by the seventh power of the linear growth factor for that redshift, $(D_+(z)/D_+(z = 0))^7$, as suggested by Pueblas & Scoccimarro (2009). In Pueblas & Scoccimarro (2009), the authors include an approximate analytic derivation of the time evolution of the vorticity power spectrum,
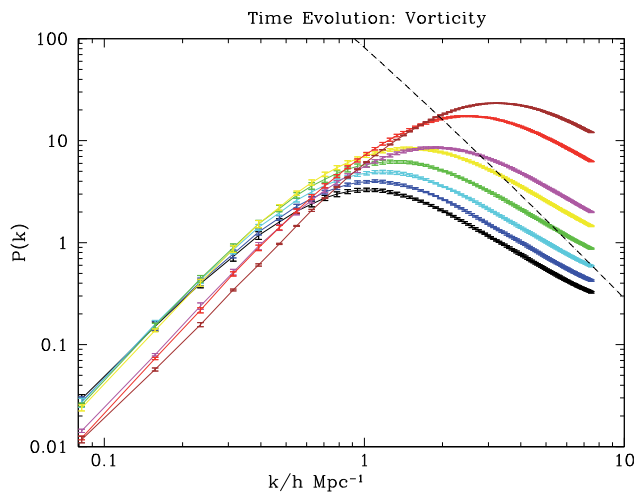
Figure B5. The non-linear vorticity power spectrum at selected redshifts, $z = 2$ to 0, each divided by the respective linear theory density growth factor to the seventh power, see Pueblas & Scoccimarro (2009). See Table 2 for details and an explanation of the colours. As expected, the linear theory prediction works well on the largest scales and is generally worse for smaller scales and later times; however, the scaling as the seventh power of the density growth factor seems to break down at earlier times. The error bars on this plot show the standard error on the mean for each set of realizations.

finding it to behave as $f_v^2(z)D_+^6(z)$), where $f_v(z)$ is the fraction of the volume that undergoes orbit crossing. Fitting to their simulations, they found $(D_+(z)/D_+(z = 0))^{7\pm0.3}$ to be the best-fitting value. The scaling of our vorticity spectrum appears similar to that found in Pueblas & Scoccimarro (2009). However, in our simulations this scaling appears to break down for higher redshift, $z \geq 1$. We see a smaller vorticity spectrum at these times than expected from the $(D_+(z)/D_+(z = 0))^7$ scaling. Fig. B5 shows this discrepancy along with the error amongst our simulations. These errors do not appear sufficiently large to explain the discrepancy. However, it is worth noting that the variation amongst our realizations (see Appendix B4) is large enough to explain the difference in the time evolution of the vorticity between our simulations and the single HR simulation in Pueblas & Scoccimarro (2009). The variation between realizations was not considered in Pueblas & Scoccimarro (2009); however, it seems likely that the function $f_v(z)$ varies between realizations. The range of the scaling of the vorticity with the linear growth factor has an upper value of 7.3 in Pueblas & Scoccimarro (2009). Using this value reduces, but does not remove the discrepancy.

B3 Comparison with the POWMES density power spectrum

The density and density gradient power spectra (the latter divided by k^2, see the consistency check above) that we have extracted can be compared to the density field extracted by POWMES (Colombi et al. 2009), a state-of-the-art conventional density power spectrum estimator. For the HR simulations, the power spectra agree within 10 per cent for $0.2\,h\,\mathrm{Mpc}^{-1} \leq k \leq 7.0\,h\,\mathrm{Mpc}^{-1}$, see Fig. 3 in file CC, and within 5 per cent for the majority of this range. A similar result is seen for the ratio of the DTFE gradient of the density spectrum (divided by k^2) to the POWMES density spectrum, see Fig. 4 in file CC.

The agreement on the largest scales, in the first four to five bins, is affected by the choice of binning. If the number of bins used for the DTFE extraction is doubled, then the DTFE and POWMES extractions agree much more closely as the bins are then of a more similar size and location. As noted in Appendix B7, if we increase the number of bins, then the number of k modes contributing to the first few bins is much smaller, so we will continue to use $N_{\mathrm{grid}}/4$ bins in our analysis. The agreement between the POWMES and DTFE methods is sufficient to support the robustness of our density and density gradient spectra.

B4 Realizations

In this section, we show how the extracted spectra vary amongst realizations. We will illustrate this with the 160 h^{-1} Mpc 640³ particle simulations for which there are eight realizations. In all cases, we consider the variation at redshift zero.

We examined the variation amongst realizations for the density field, using both the DTFE code and POWMES, and also the velocity divergence. These all showed the expected variation, namely that cosmic variance causes a difference between the realizations on the largest scales in each box, but this difference is much reduced on smaller scales. The variance between realizations for the density field was very similar for the two methods of extracting the density field.

In Fig. B6, we show the variation of the vorticity field amongst realizations. This plot shows that the variation amongst realizations is greater for the vorticity than for the density. On smaller scales, the variation amongst realizations of the vorticity is less than that on large scales, but still greater than that for the density field. We are not aware of this being previously noted in the literature, and the works (Pueblas & Scoccimarro 2009; Zheng et al. 2013; Hahn et al. 2014) that we compare our vorticity spectrum to in the main text do not have multiple realizations in order to have seen this effect.

In Fig. B7, we show the variation amongst realizations of the vector potential. On large scales, the variation between realizations is very similar to that between the vorticity spectra. However, the variation does not appear to reduce on smaller scales. According to perturbative results (Lu et al. 2008; Hui-Ching Lu et al. 2009), the vector is generated most efficiently by coupling between two different k modes, particularly if one of them is entering the horizon. Given the similar qualitative behaviour of the fully non-linear vector potential, it is
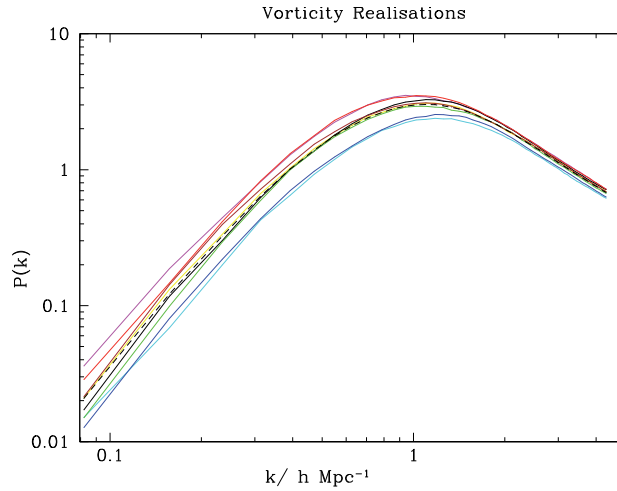
Figure B6. The vorticity power spectra as extracted from the eight 160 h^{-1} Mpc simulations with 640^3 particles. The dashed black line denotes the average of the eight simulations.
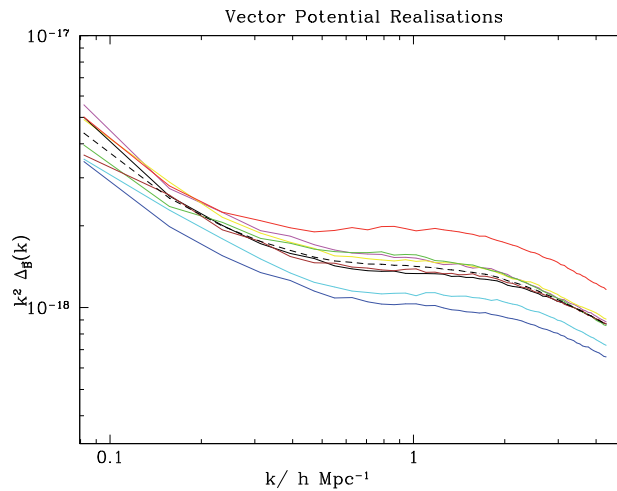

Figure B7. The vector potential power spectra as extracted from the eight 160 h^{-1} Mpc simulations with 640^3 particles. The dashed black line denotes the average of the eight simulations. The spectra have been multiplied by k^2 in order to better show the variation.

reasonable to assume that this is also generated by coupling between large-scale modes and small-scale modes. Thus, the large-scale variance between realizations will be affecting the vector power spectrum on smaller scales, resulting in the variance between realizations not decreasing on small scales.

In Fig. B8, we show how the value of the vector potential from the individual realizations of the HR simulations compares to the average over realizations of simulations with different parameters. Note that the variation between the HR realizations is greater than the variation between the average over realizations for different simulation parameters.

As mentioned above, the increased variance between realizations may be an unavoidable feature of the vector potential. As such, this represents the dominant source of error in calculating the vector potential, as long as the simulation parameters are sufficiently good. If an observational test of the vector potential was found, then many more realizations than the number carried out for this paper would be required, in order to more carefully investigate this effect and determine more precisely what the observational prediction would be for a ΛCDM cosmology.

B5 Softening length

In this paper, we have chosen our softening lengths following Pueblas & Scoccimarro (2009) in order to compare to their results. In Fig. B9, we show how a 160 h^{-1} Mpc simulation with 640^3 particles and the same initial conditions varies if the softening length changes from 6.5 to 5 kpc. This is a 20 per cent change in the softening length. The variation between the density, velocity divergence and vorticity spectra is very small for this change. The power spectrum of the vector potential varies more, but is within 5 per cent of the value for nearly the entire range under consideration. Since this 5 per cent variation is significantly smaller than the 20 per cent variation in the softening length, we do not think the choice of softening length significantly impacts our results for a sensible choice of softening length.
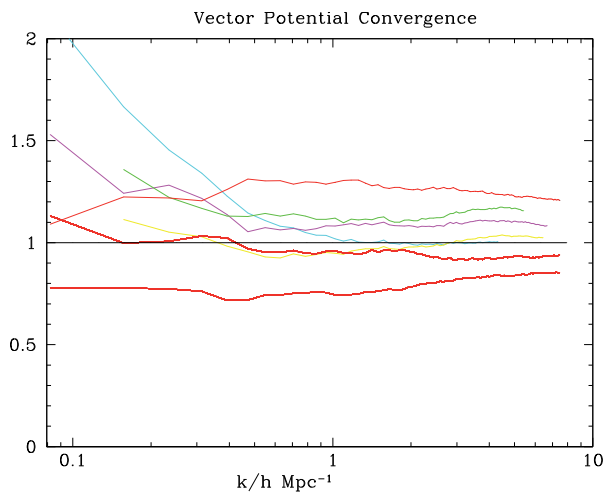
Figure B8. The vector potential power spectra from different simulations, divided by the average vector potential from the three 160 h^{-1} Mpc simulations with 1024^3 particles. The three red curves show the vector potential from the three realizations of the 160 h^{-1} Mpc simulations with 1024^3 particles. The cyan and magenta curves show the vector potential from the average of the 160 h^{-1} Mpc simulations with 640^3 and 880^3 particles, respectively. The yellow curve shows the average of the 140 h^{-1} Mpc simulations with 768^3 particles and the green curve shows the average of the 200 h^{-1} Mpc simulations with 1024^3 particles. Note that the variation between the HR simulations is greater than the variation between the average values from simulations with different parameters.
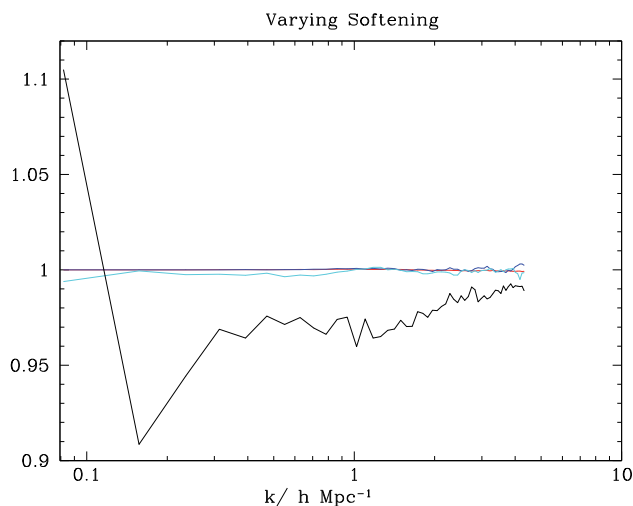

Figure B9. The ratio between the power spectra extracted at redshift zero for the same initial conditions run with two different softening lengths. The different spectra plotted are density (red), velocity divergence (blue), vorticity (cyan) and the vector potential (black).

B6 Smaller boxes

Here we examine some additional plots that demonstrate some of the comments made in the main text. We ran a set of eight simulations with 512^3 particles in an 80 h^{-1} Mpc box and extracted the power spectra in the same way as from our other simulations. In Figs 3, 5 and 6 in file RB, we show the density, vorticity and vector potential power spectra, respectively, colour coded to match box size as in Fig. B3. In addition, the power spectra extracted from the smaller boxes are shown as a dashed black line. It is clear that the spectra extracted from the smaller 80 h^{-1} Mpc boxes are systematically smaller, irrespective of any other dependence on box size and resolution. The effect of using (too) small boxes when running *N*-body simulations has been examined in the past, see e.g. Gelb & Bertschinger (1994), Bagla & Ray (2005) and Bagla & Prasad (2006). A suggestion in Bagla & Prasad (2006) is that it is important that the ratio between the box size and the scale of non-linearity is sufficiently large. As a result, for our simulations, the smallest boxes we have run that we consider trustworthy are the 140 h^{-1} Mpc simulations. It remains to be seen whether smaller boxes, such as the 100 h^{-1} Mpc simulations used in Zheng et al. (2013), are a robust source of spectra such as the density and vorticity.

B7 Number of bins

We considered the effect on our extracted power spectra of varying the number of bins. As expected, increasing the number of bins increases the noise of the power spectra and there is no systematic deviation. Our results from varying the number of bins on the density, velocity divergence and vorticity power spectra are shown in Figs 4–6 in file GB. In each of these plots, the 256 bins used for the analysis in this

paper are shown by the black line, the blue line denotes the use of 512 bins and the red line is for 1024 bins. We have used 256 bins for our analysis to ensure that the low-k bins contain a sufficient number of k modes. For the 256 bins, the first two k bins contain 58 and 218 k modes, respectively, whereas these numbers are 12 and 41 for the corresponding bins when 1024 bins are used. Note that, as mentioned in the POWMES section, the variation between the 256-bin and 512-bin power spectra is similar to the variation between the POWMES method and the DTFE method using 256 bins. This is due to the number and location of bins in the POWMES method being very similar to the DTFE method with 512 bins.

In addition, Fig. 7 in file GB shows the variation of the vector potential power spectrum with the number of bins. Again, the change in the number of bins is negligible. In this plot, the dashed lines show the power spectra computed with the extra factors of k explicitly included whilst summing over the modulus-squared values of the field; see the velocity consistency check for more information. As expected, this change affects things the most in the largest bins and therefore on large scales and for the smallest number of bins; however, it does not affect our results.

This paper has been typeset from a TEX/LATEX file prepared by the author.